

# Spectral Downscaling of Integrated Water Vapor Fields From Satellite Infrared Observations

Mario Montopoli, Nazzareno Pierdicca, and Frank S. Marzano, *Senior Member, IEEE*

**Abstract**—Atmospheric water vapor is a crucial constituent affecting both climate change and hydrological cycle processes, whereas on the other hand, it has a significant impact on the electromagnetic signal propagation. Since the distribution of atmospheric water vapor strongly varies with time, location, and altitude, it is necessary to monitor it at high spatial and temporal resolution. Unfortunately, mapping its spatial distribution is difficult due to the lack of meteorological instrumentation at an adequate spatial and temporal observation scale. For many geophysical applications, there is also the need to reconstruct spatial details of integrated precipitable water vapor from information available only at coarser spatial scales. Spatial downscaling approaches can play a significant role when high-resolution water vapor retrievals from relatively new sensors, like synthetic aperture radars, or from conventional sensors, like the infrared radiometers Medium Resolution Imaging Spectrometer (MERIS) or Moderate Resolution Imaging Spectroradiometer (MODIS), are used in synergy to enhance the accuracy of integrated water vapor retrievals. In this context, this paper introduces some new methodological aspects to increase the spatial resolution of integrated precipitable water vapor observations using a statistical downscaling spectral approach. To highlight the potential and the usefulness of the proposed downscaling estimation procedure, collocated 250-m MERIS and 1-km MODIS acquisitions are used. Results reveal the ability of spectral downscaling to reproduce quite well the second-order statistical variability of the water vapor field at small spatial scales with a root-mean-square error comparable with conventional interpolation techniques.

**Index Terms**—Downscaling, Earth observations, remote sensing, satellite observations, statistical interpolation, water vapor.

Manuscript received November 10, 2010; revised May 20, 2011; accepted July 3, 2011. Date of publication August 8, 2011; date of current version January 20, 2012. This work was supported in part by the European Space Agency under Contract N. ESTEC 21207/07/NL/HE and in part by the Abruzzo Region, Italy.

M. Montopoli is with the Department of Electrical and Information Engineering and the Center of Excellence Centro di Eccellenza per l'integrazione di Tecniche di Telerilevamento e Modellistica Numerica per la Previsione di Eventi Meteorologici Severi, University of L'Aquila, 67040 L'Aquila, Italy (e-mail: mario.montopoli@univaq.it).

N. Pierdicca is with the Department of Information, Electronic and Telecommunication Engineering, Sapienza University of Rome, 00184 Rome, Italy (e-mail: pierdicca@die.uniroma1.it).

F. S. Marzano is with the Department of Information, Electronic and Telecommunication Engineering, Sapienza University of Rome, 00184 Rome, Italy, and also with the Center of Excellence Centro di Eccellenza per l'integrazione di Tecniche di Telerilevamento e Modellistica Numerica per la Previsione di Eventi Meteorologici Severi, University of L'Aquila, 67040 L'Aquila, Italy (e-mail: marzano@die.uniroma1.it).

Color versions of one or more of the figures in this paper are available online at <http://ieeexplore.ieee.org>.

Digital Object Identifier 10.1109/TGRS.2011.2161996

## I. INTRODUCTION

IT IS well known that atmospheric water vapor is a crucial constituent affecting climate and precipitation processes, and at the same time, it has a significant impact on both the amplitude and phase of electromagnetic signals propagating through the atmosphere. Since the distribution of atmospheric water vapor strongly varies with time, location, and altitude, it is necessary to monitor it at high spatial and temporal resolution. Improved knowledge of the water vapor field is important for weather forecast models, as well as to correct path delay errors in Global Positioning System (GPS) and interferometric synthetic aperture radar (SAR) (InSAR) geodetic applications. Unfortunately, the estimation of integrated precipitable water vapor (IPWV) maps from satellites can suffer from poor spatial resolution. This is quite evident when using satellite microwave radiometers on low-Earth-orbit platforms, which have a resolution, at 22 GHz, on the order of  $50 \times 50 \text{ km}^2$ . Examples of these radiometers are the Special Sensor Microwave Imager on the Defense Meteorological Satellite Program platforms, the Advanced Microwave Scanning Radiometer Enhanced (AMSR-E) on the Aqua and Terra platforms, and the Advanced Microwave Sounding Unit A (AMSU-A) on the National Oceanic and Atmospheric Administration and METeorological OPERational platforms [1]–[3]. The spatial variability of the water vapor field can be fairly high within the instrument footprint. A partial improvement, in this respect, is obtained when using a satellite infrared radiometer, such as the MEdium Resolution Imaging Spectrometer (MERIS) aboard ENVIRONMENTAL SATellite and the Moderate Resolution Imaging Spectroradiometer (MODIS) aboard the Aqua platform, which have a resolution of  $300 \text{ m}^2$  and  $1 \times 1 \text{ km}^2$  [4], [5], respectively, over land and during daylight. The infrared retrieval drawbacks are that the integrated water vapor is generally limited to the middle-top troposphere, thus discarding the boundary layer contribution, or they are limited to daylight conditions.

A novel and very promising technique to map water vapor, or at least its variation with time, at high spatial resolution is presented by InSAR. When measuring backscatter from coherent permanent scatters (PSs) above a stable earth surface, a sequence of multipass SAR interferograms provides information on the atmospheric phase screen (APS). The APS maps at high resolution the difference in electromagnetic path delay between passes which is mainly determined by the varying water vapor content along the slanted path from PSs to radar [26]. On the other hand, InSAR acquisitions for Earth monitoring purposes, at spatial resolutions on the order of tens of meters, can be seriously affected by the additional signal path delay induced by the atmospheric water vapor distribution, which can cause incorrect interpretations, when InSAR is used to derive digital

elevation models (DEMs) or to detect surface displacements. In this context, independent information on water vapor on spatial scales comparable to those obtained by SARs can be of some utility to distinguish atmospheric phase changes in the interferogram from those due to the earth surface changes. Past work has attempted to mitigate atmospheric impairments from InSAR acquisitions. In [32], a GPS receiving network is used, together with the Taylor's frozen flow hypothesis, to obtain higher resolution maps of integrated water vapor. The same goal is pursued using space-based sensors in [4] and [33] where retrievals of integrated water vapor from MERIS are used. Other sensors from satellite platforms (e.g., MODIS or AMSU-A and AMSR-E when available) can be, in principle, used, but in this case, the lower spatial resolution may be a limiting factor for effectively mitigating water-vapor effects on InSAR.

The increasing spatial resolution of current numerical weather prediction (NWP) models has to be also mentioned, which demand the same resolution input data used as initial condition and observations to be assimilated. High-resolution observed water vapor maps are certainly very important also in this application field.

A way to approach the lack of information at small spatial scales may be to resort to spatial field downscaling (also called disaggregation). In general, a downscaling procedure is aimed at reconstructing the observed field (which has a coarser resolution both in time and space) at unresolved spatial or temporal scales or, in other words, at estimating details that were not available in the original observed field. The concept behind this approach is that the large-scale field can be considered as a boundary condition to the small-scale field, and if the field's spatial autocorrelation or spectral density is known, then the small-scale field can be reconstructed, at least on the average. This approach has been already used for the rainfall field at the ground [6] in order to enhance the spatial resolution of the weather forecast rain rate at "reliable" scales, which are on the order of tens of kilometers, to hydrological scales, which are on the order of kilometers, or even less.

Interpolation is another way to estimate a field at locations at which its value is unknown and to increase the number of samples. As opposed to downscaling, it is based on a minimum root-mean-square error (rmse) criterion, and it is generally not capable of increasing the range of high spatial frequency components of the observed field, i.e., of reconstructing smaller scale features.

Downscaling studies are rarely applied to humidity, although its small-scale spatial distribution may strongly affect cloud convection parameterization and climate change models. Some references can be found in [7], [24], [25], and [34]. Two downscaling methodologies may be, in general, considered among downscaling approaches: 1) fractal downscaling [8] and 2) spectral downscaling [9]. The assumption behind fractal geophysical downscaling is that there is spatial correlation among the various field scales. In other words, the spatial field is supposed to be fractal or multifractal, and the characteristic of the handled field can be disaggregated by repeating previously identified large-scale features at smaller scales. Spectral downscaling, on the other hand, is based on the principle that the spatial field at a given scale may be extrapolated to small scales

by properly modeling its spatial properties at any observable scale in the Fourier transformed domain. The generation of multidimensional random fields at small scales by spectral downscaling has a long history in hydrology [1], [10]–[12]. An effective approach is to adopt a spectral model to generate a 2-D isotropic random field by taking the inverse Fourier transform of a spectrum with an assigned amplitude distribution and a random Fourier phase. Since it is relatively practical and in order to directly include spatial information into the downscaling procedure, the spectral approach is preferred over the fractal approach.

In this paper, an analysis of water vapor spatial properties at different scales is performed using different measurement techniques, and an original methodological approach for downscaling water vapor fields is proposed. Microwave and infrared radiometers, GPS data, InSAR APS high-resolution maps, and outputs of NWP models are considered. A mathematical formulation is developed to compare downscaling and geostatistical interpolation methods. From this formulation, a new approach to setting the phase of higher frequency components within a spectral downscaling approach has been introduced, as opposed to setting them randomly. The proposed spectral approach is firstly used on the reference MERIS IPWV retrievals and secondly tested on MODIS and MERIS retrievals, at 1- and 0.25-km horizontal spatial resolutions, respectively, to simulate an operational framework where high-resolution maps of IPWV are obtained, after downscaling, from lower resolution maps provided by a variety of sensors. In fact, this work was accomplished within a project funded by the European Space Agency (ESA) aiming to mitigate the tropospheric artifacts on InSAR interferograms with resolution on the order of a few tens of meters.

This paper is organized as follows. In Section II, the spatial characterization of water vapor fields is carried out using available data and variogram analysis. In Section III, the spectral spatial downscaling method is described, and in Section IV, it is applied both to MERIS data for self-consistency tests and to MERIS and MODIS IPWV retrievals. Conclusions are drawn in Section V, while the appendixes discuss some relevant details.

## II. SPATIAL CHARACTERIZATION OF WATER VAPOR FIELDS

In this section, features of water vapor fields are extracted and analyzed, using variogram analysis of data produced by many different sources. The variogram is a commonly used tool in geostatistics to investigate spatial variability at different scales.

### A. Data Description

During September and October 2008, as a part of the ESA Mitigation of Electromagnetic Transmission errors induced by Atmospheric Water Vapor Effects (MetaWave) project [13], an experimental campaign has been conducted, and several types of data have been collected to characterize the water vapor field. The selected target area was that of Central Italy, in the urban area of Rome. Among other observations, the collected data included: time series from a network of GPS

TABLE I  
LIST OF AVAILABLE OBSERVATIONS DURING THE META WAVE CAMPAIGN

	Year	Month and Day	Temporal Resolution	Spatial Res. [km]
<b>MM5</b>	94	1, 16 Jan.; 6 Feb.; 26 Mar.; 7,10 Apr.	1 hour	1
	08	17, 20, 23,24, 26,27,29,30 Sept; 02-03 Oct.	1 hour	1
<b>Terra</b>	08	23-30 Sept.; 1-7 Oct.	1 day	1
<b>Aqua</b>	08	23-30 Sept.; 1-7 Oct.	1 day	1
<b>MERIS</b>	08	20-30 Sept.; 2-3 Oct.	3 day	0.25
<b>Radar SAT</b>	03, 07	2003-2007	30 day	0.1
<b>ASAR</b>	02, 08	2002-2008	20 day	0.1
<b>ERS-1</b>	94	Jan. to Apr.	3 day	0.1
<b>GPS</b>	08	20-30 Sept. 01-04 Oct.	0.5 hour	-

receivers, MERIS and MODIS products from Terra and Aqua sensors, and the Advanced SAR (ASAR) acquisitions aboard ENVISAT. Launches of radiosounding balloons and deployment of ground-based microwave radiometers were also part of the experiment. From each remote sensing data source, the IPWV field has been made available, either as a delivered high-level product or by processing low-level products using proper retrieval algorithms. In particular, a sequence of InSAR acquisitions has been processed using the PS technique by the Polytechnic University of Milan to produce the so-called APS [26]. The GPS receiver data, collected from the operational network, have been processed using the Bernese software [27] to provide the zenith total delay (*ZTD*) estimates, from which the zenith wet delay (*ZWD*) has been derived by subtracting the dry contribution to the path delay using the Saastamoinen model [28], and surface pressure and temperature operational measurements.

Numerical simulations of IPWV have been considered as well, using the Mesoscale Model 5 (MM5) numerical weather forecast model, which has been run during the same days as the experimental campaign. Table I lists the measurements that are available for this study, together with some of their features. A DEM of the target area was also used to account for the deterministic variation of the IPWV above the Earth’s surface at different heights.

In order to strengthen the subsequent spatial analysis, additional observations and simulations have been considered in comparison to those collected during the experimental campaign. They are additional sequences of APS maps from RadarSat and the Environment Remote Sensing 1 (ERS-1) satellites. They are listed in Table I as well.

*B. Spatial Analysis*

All data listed in Table I have been used to characterize the spatial behavior of water vapor at a variety of spatial scales from a few meters to a dozen kilometers. To this end, acquisitions from remote sensors, usually provided in terms of ZWD from GPS receivers and APS from SAR, have been previously converted into integrated precipitable water vapor, expressed in centimeters [4]. The level 2 products from MERIS

and MODIS providing IPWV have been used as such [29]. After those dimensional conversions, the semivariogram has been extracted from each data source.

The semivariogram, under the second-order spatial stationarity hypothesis, is defined as follows [14]:

$$\gamma_V(\mathbf{l}) = \frac{1}{2} \cdot \left\langle \left( \tilde{V}(\mathbf{r} + \mathbf{l}) - \tilde{V}(\mathbf{r}) \right)^2 \right\rangle \quad (1)$$

where  $\gamma_V$  indicates the semivariogram of integrated precipitable water vapor,  $V$  identifies each available source of information, and  $\mathbf{l}$  (in kilometers) is the lag distance vector between two points at positions  $\mathbf{r}$  and  $\mathbf{r} + \mathbf{l}$ , whereas the symbol  $\langle \cdot \rangle$  stands for the average operator in the spatial domain. To avoid misrepresenting the spatial features of water vapor and to agree with the stationarity hypothesis as much as possible, the trend of  $V(V_T)$ , that is the nonstationary component of the field being a function of the terrain height ( $h$ ), has been modeled with an exponential function of parameters  $v_0$  and  $k$  of the type  $V_T(\mathbf{r}) = v_0 \exp(-k \cdot h(\mathbf{r}))$  (e.g., as done in [15] and [16]) and then removed from each source of data. This leads to the detrended integrated precipitable water vapor, indicated by the tilde over  $V$ . The definition of  $V_T$  through its parameters  $v_0$  and  $k$  can be achieved using a network of GPS stations well distributed over the domain of interest in order to cover the whole dynamic range of the terrain height  $h$ .

Indeed, the various variogram shapes (i.e., gently increasing as compared to abruptly increasing curves saturating after a given lag) could be due not necessarily to the characteristic features of the water vapor field, but instead to a distinctive response of the considered data acquisition sensor, such as noise, resolution, and so on. In order to deal with an unbiased comparison among variograms, the need to reduce the effect that the sensor spatial filtering has on the relative variogram is crucial. For this reason, we have applied a normalization procedure, described in Appendix A, which is fundamental when dealing with variograms derived from different data sources.

Under the spatial isotropy hypothesis, Fig. 1 shows the result of the variogram analysis.

As already concluded in past studies (e.g., [17]), the analysis of Fig. 1 shows that the power law model can describe quite

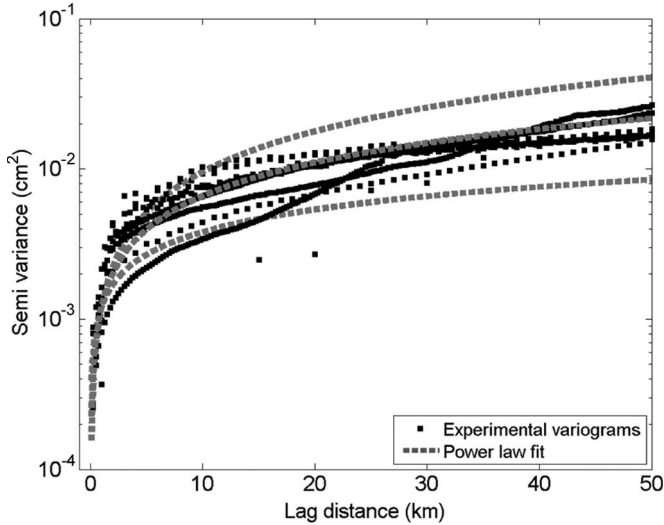


Fig. 1. Normalized semivariograms from various sources of measured data. Dotted curves represent the power law model of type  $\gamma = \alpha \cdot l^\beta$ , with  $\alpha$  and  $\beta$  being coefficients equal to  $\beta = 0.76$ ,  $\beta = 0.90$ ,  $\beta = 0.60$ , for the middle, upper, and lower dotted curves, respectively, and  $\alpha = 0.0012$ , a value common to the three models. Note that the best fitting of the experimental variograms after normalization gave  $\beta = 0.76$ .

well the semivariograms of IPWV assuming as an isotropic function of the lag distance (see the dotted fitting curves)

$$\gamma_{PL}(l) = \alpha \cdot l^\beta \quad (2)$$

where  $l$  is the scalar lag distance in polar coordinates (see Appendix B) and  $\alpha$  and  $\beta$  are regression parameters which represent respectively the characteristic scale of the process and the rate at which the autocorrelation of the water vapor, supposed to be a random function, decreases with increasing lag distance.

By performing a best fit of the empirical semivariograms of the data sources, it has been found that  $\beta = 0.76$  (i.e., it approaches the theoretical Kolmogorov law of  $2/3 = 0.67$ ) and  $\alpha = 0.0012$  which seems to agree with the Kolmogorov theory of turbulence [18]. Such a model has been shown as the middle dashed curve in Fig. 1. Upper and lower dashed curves are obtained with  $\beta = 0.9$  and  $\beta = 0.6$ , respectively, and  $\alpha = 0.0012$ . It is worth mentioning that the best fit of the semivariograms in Fig. 1 may suffer from significant errors at lower lag distances due to the lack of information at finer spatial scales which, in turn, are the scales that we want to reconstruct. The downscaling procedure described in Section III is aimed to reconstruct such scales by extrapolating from larger ones. Additionally, it should be mentioned that the parameters  $\alpha$  and  $\beta$  in (2) are, in principle, dependent on space and time in order to take into account the variability of water vapor. Thus, for operational use, time series of additional measurements (i.e., GPS and/or satellite radiometers), even if at large scales, are needed to estimate  $\alpha$  and  $\beta$  within the desired space time domain.

It should be additionally mentioned that, for differential InSAR (dInSAR) observations, representing differences between two different times and supposed to be independent of each other, the corresponding semivariogram must be divided by a

factor of two to be compared with the semivariograms derived from other types of observations (see Appendix A for details).

As will become clear in the next sections, from the downscaling point of view, it is fundamental to describe the spatial variability of  $V$  in terms of power spectra, instead of semivariograms. In this respect, two approaches are possible. The first approach foresees the direct computation of power spectra using the Fourier transform of available observations. However, this operation is not easily applied since the 2-D Fourier operator requires the availability of a regularly sampled field. A second approach consists of deriving the power spectra from semivariograms, which, in turn, do not require any particular constraint on data sampling.

As a matter of fact, under the field stationarity and isotropy assumptions and considering the power law relation for describing the variograms, we have found that the modulus of power spectra ( $\phi$ ) and the semivariogram model  $\gamma_{PL}$  in (2) are related to each other through the Hankel transform so that the following applies:

$$\phi(s) = 2\pi \cdot \left[ \frac{C_1(a, b)}{(s^2 - a^2)^{b+1}} \right] \approx s^{-\nu} \quad \text{for } s \gg a \quad (3)$$

where  $s = \lambda^{-1}$  is the spatial frequency,  $\lambda$  is the spatial wavelength, and  $a$  and  $b$  are coefficients related to  $\alpha$  and  $\beta$  introduced to facilitate the derivation of (3) from (2), whereas  $\nu = 2b + 2$  and  $C_1$  is a constant. Details for deriving the power spectra from the semivariogram are discussed in Appendix B. As we can see from (3),  $\phi$  increases as the  $\nu = (2b + 2)$  inverse power for  $s \gg a$ . The power spectral model that we just formalized will be used in the downscaling process, discussed in the next section.

An empirical model with  $\beta = 0.76$  and  $\alpha = 0.0012$  results in coefficients  $b$  and  $a$ , respectively, with values of 0.37 and  $0.19 \cdot 10^{-7}$ .  $C_1$  and  $\nu = (2 \cdot b + 2)$  are  $-9.34 \cdot 10^{-4}$  and 2.74, respectively. In particular, the value  $\nu = 2.74$  is very close to  $8/3 = 2.67$  resulting from [19].

### III. SPECTRAL SPATIAL DOWNSCALING

The downscaling algorithm is based on the description of the complex Fourier spectrum ( $F_V$ ) of the integrated water vapor field at unresolved scales. This description, of course, includes both the spectral amplitude  $A_V$  and the Fourier phase  $\Psi_V$  related to  $F_V$  as follows:

$$F_V(\mathbf{s}) = A_V(\mathbf{s}) \cdot e^{-j \cdot \Psi_V(\mathbf{s})} \quad (4)$$

where  $\mathbf{s}$  is the 2-D spatial frequency. It is valuable to remember that the spectral amplitude is related to the power spectral density (PSD) by the following relation:

$$\phi_V(\mathbf{s}) = \langle |F_V(\mathbf{s})|^2 \rangle = \langle [A_V(\mathbf{s})]^2 \rangle \quad (5)$$

where  $\langle \cdot \rangle$  is the expectation operator and  $|\cdot|$  indicates the modulus of a complex number. Spatial-spectral downscaling assumes that the whole range of spatial scales of a scalar field is split into a known scale  $s_{kn}$  within the interval  $kn$  of the spatial frequency domain and an unknown scale  $s_{un}$  within domain

$un = \mathcal{R} - kn$ , where  $\mathcal{R}$  is the  $C_2$  space. After expressing the Fourier transform  $F_V$  for the whole range of scales, the inverse Fourier transform is taken to recover the downscaled field  $V_d$

$$V_d(\mathbf{r}) = \mathfrak{S}^{-1} \{F_V(\mathbf{s})\} = \mathfrak{S}^{-1} \{F_{V_{kn}}(\mathbf{s}_{kn}) + F_{V_{un}}(\mathbf{s}_{un})\} \quad (6a)$$

where  $\mathbf{r}$  is the 2-D position vector and  $F_{V_{kn}}$  and  $F_{V_{un}}$  are the IPWV spectra at known  $\mathbf{s}_{kn}$  and unknown  $\mathbf{s}_{un}$  spatial frequencies, respectively. It is also true that  $V_d = V_{kn} + V_{un}$  with

$$\begin{cases} V_{kn}(\mathbf{r}) = \mathfrak{S}^{-1} \{F_{V_{kn}}(\mathbf{s}_{kn})\} \\ = \mathfrak{S}^{-1} \{A_{V_{kn}}(\mathbf{s}_{kn}) e^{-j \cdot \Psi_{V_{kn}}(\mathbf{s}_{kn})}\} \\ V_{un}(\mathbf{r}) = \mathfrak{S}^{-1} \{F_{V_{un}}(\mathbf{s}_{un})\} \\ = \mathfrak{S}^{-1} \{A_{V_{un}}(\mathbf{s}_{un}) e^{-j \cdot \Psi_{V_{un}}(\mathbf{s}_{un})}\} \end{cases} \quad (6b)$$

where the definitions of the symbols are evident. With (6) in mind, the downscaling problem can be solved once the Fourier spectrum  $F_{V_{un}}$  at unknown frequency scales is completely determined.

Next, the spectral amplitudes at unresolved scales ( $A_{V_{un}}$ ) can be inferred, at least in the average sense, from the empirical model of (3). Once the model parameters are correctly estimated,  $A_{V_{un}}$  can be derived through (5) as the square root of the PSD. Note that, by virtue of (5), the rate at which  $A_{V_{un}}$  decreases as the spatial frequency  $s$  increases is not  $\nu$  but  $\nu/2$ .

On the other hand, the Fourier phase  $\Psi_{V_{un}}$  can be generated at least in two ways. The first one assumes a uniformly distributed random phase (RP) generator. In doing so, several likely realizations of IPWV are provided as output of the downscaling procedure. The second method, which is the one proposed in this paper, determines the Fourier phase following a deterministic approach, i.e., setting a deterministic phase from finer scale interpolation (DPFI). It consists of taking the Fourier phase at unresolved scales from the map obtained by interpolating the coarse resolution map at the final desired finer resolution. Various interpolation algorithms can be considered to accomplish this aim, and we used the bilinear one. Of course, any IPWV map sampled at the required resolution, for example, taken from NWP models, if compatible with the observations, can be used for this purpose.

It should be noted that the downscaling approaches proposed in the past (see [6], [20], and [25]) mainly focused on the description of the term  $A_{V_{un}}$ , instead of  $\Psi_{V_{un}}$ , with the latter usually being randomly generated. As we will see in the next section, the description of the term  $\Psi_{V_{un}}$  is crucial to obtain accurate downscaled fields.

#### IV. DOWNSCALING TESTS USING SATELLITE DATA

In this section, some tests on the downscaling algorithm are performed. The first class of tests concerns the use of MERIS fields of IPWV, taken as reference, which are upscaled and subsequently downscaled at the same resolution as that of the reference MERIS field to verify the self-consistency of the downscaling procedure. The second test is a direct application to satellite measurements during the MetaWave campaign (see Table I) in which a MODIS acquisition at 1 km has been

downscaled and compared with the reference MERIS IPWV field at 0.25 km.

##### A. Self-Consistency Tests of the Downscaling Algorithm

In order to verify the goodness of the downscaling approach, a self-consistency test has been set up. A MERIS observation acquired on September 29, 2008, at 09:50 UTC and with a spatial resolution on the order of 250 m was taken as a reference frame. Then, it was upscaled by a given upscaling factor (UF) to obtain a coarse resolution field from which the downscaling procedure was run using a downscaling factor (DF). The resulting downscaled field was then compared to the initial MERIS acquisition. The self-consistency test just described is shown schematically in Fig. 2, where the power spectrum at resolved (bold line) and unresolved (dashed line) scales is shown in the lower left corner. The upscaled field has been obtained by smoothing the high-resolution field by applying a local spatial average operator.

Tests are performed by taking a linear model in log scale for the power spectra at unresolved scales with slope  $\nu = 2.84$ , consistently with (3), as suggested by the spatial characterization analysis that was previously discussed. Note that the slope  $\nu$  has been estimated from the variogram analysis performed for the considered case study on September 29.

Fourier phases are chosen according to various criteria: RP, deterministic phase from finer scale interpolation of the upscaled MERIS at coarse scale (DPFI), which is the approach introduced in this paper, and, finally, deterministic phase from the reference MERIS field at 250 m (DPMRS). This choice has been included as a reference lower bound for the downscaling error for the other cases.

The results of this analysis are shown in Fig. 3 in terms of rmse and correlation coefficient (CC) with respect to the original MERIS map as a function of the DF. The DF is defined as the (integer) number expressing the ratio between the spatial resolution of the original and downscaled maps (note that if  $DF < 1$ , it becomes a UF). In most cases, as the DF increases, the rmse increases and the CC decreases. In addition, as expected, when the chosen phase equals that extracted directly from the MERIS reference, the best scores are obtained (i.e., the lowest rmse and highest CC). On the other hand, when the RP is considered, higher errors are noted: The presence of multiple curves is due to the generation of 30 realizations with RP. A compromise between the aforementioned two cases is represented by the DPFI choice, which is the one that we propose in this paper, where the Fourier phase at unresolved scales is taken from the map obtained by resampling the coarse resolution map at the final desired finer resolution using a bicubic interpolation.

On the other hand, as mentioned in the introduction, interpolation provides values of the field at virtually any position to directly build an oversampled map at a given DF. Therefore, it is worth comparing the downscaling technique with a simple bilinear interpolation approach, whose results are also reported in Fig. 3. From the figure, it can be noticed that, in fact, interpolation provides scores much better than the standard downscaling with RPs and even slightly better than the spectral

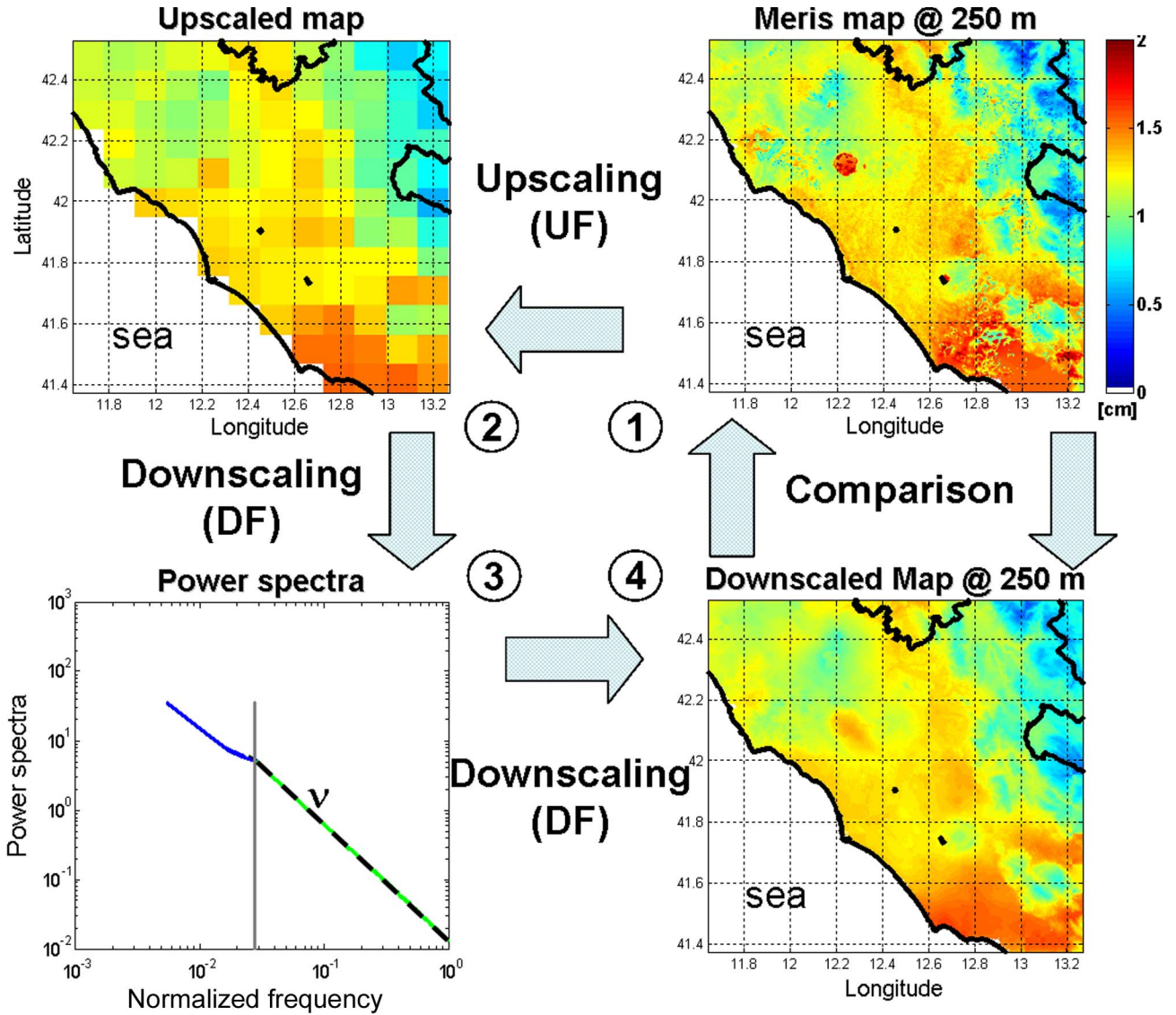


Fig. 2. Downscaling self-consistency test qualitative scheme. The vertical bar in the lower left panel indicates the separation between large-scale and small-scale components of the frequency spectrum.

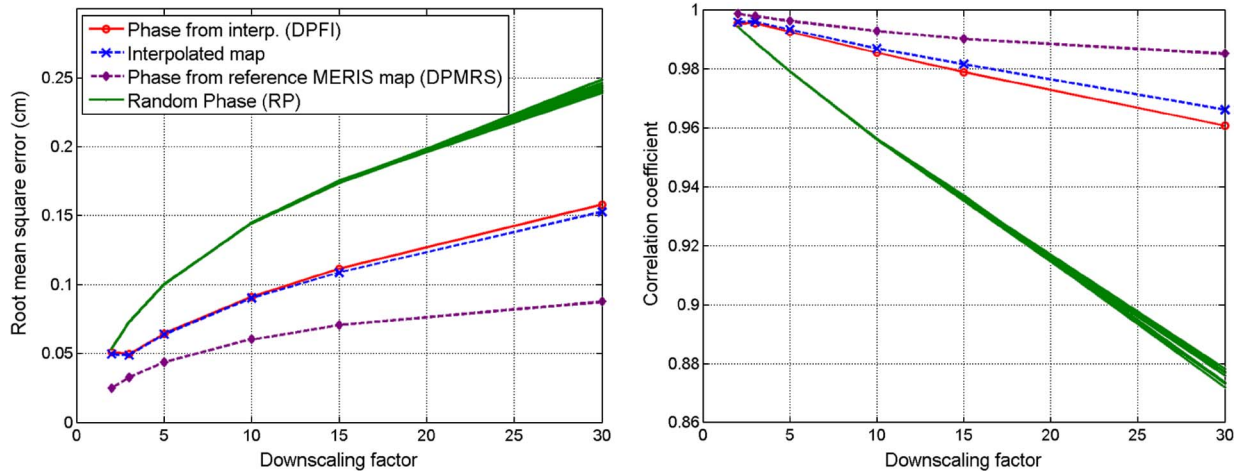


Fig. 3. Scores (left panel: rmse; right panel: CC) for downscaling self-consistency tests. Green curves (-): Score associated with 30 realizations with RP. Red curve (o): Scores obtained using Fourier phase from bicubic interpolation of upscaled field at finer scales. Blue curve (x): Scores obtained directly using bicubic interpolated field as downscaled one. Violet curve (diamond): Scores obtained using Fourier phase directly from MERIS at finer scale.

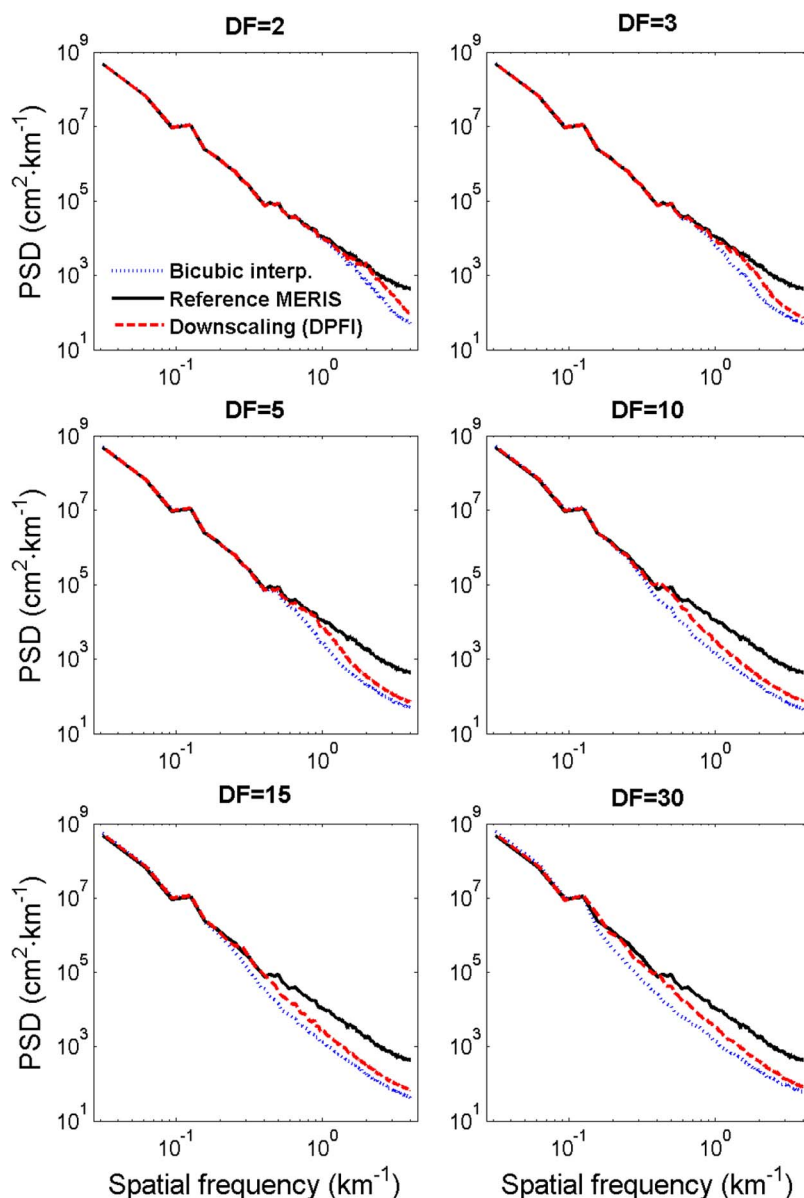


Fig. 4. Radial averages of 2-D PSD (black solid line) from MERIS, (red dashed line) downscaled with deterministic phase, and (blue dotted line) using bicubic interpolation. Each subplot refers to a specific DF from 2 to 30 as indicated in the panel's title.

DPFI downscaling proposed here, at least when using rmse and CC as quality factors.

If the comparison moves to higher order statistical moments, instead of the first order (i.e., rmse and CC) as has been done so far, the results reveal interesting features. Fig. 4 shows the second-order statistic of the MERIS map at 250 m (black solid lines), downscaled map in the DPFI case (red dashed lines), and the interpolated map of detrended IPWV (blue dotted lines), in terms of radial averages of 2-D PSD. At smaller spatial scales (i.e., higher spatial frequencies), the downscaling DPFI procedure proposed here tends to be closer to the reference values (i.e., the MERIS map at 250 m) than the interpolated field does, for all considered DFs ranging from 2 to 30. On the other hand, for large spatial scales, the agreement between all curves is excellent since all methods are able to preserve the large-scale properties. This result is encouraging since, when PSD at unresolved scales (i.e., scales which were not

known before running the downscaling procedure) is correctly modeled, some benefits at small scale are obtained. In summary, Figs. 3 and 4 suggest that the DPFI downscaling procedure tends to represent the second-order statistics better than other options, whereas the first-order statistics are comparable with the results obtained by direct interpolation.

Finally, in Fig. 5, a qualitative comparison between the aforementioned methods is shown. A snapshot of the reference MERIS map (upper left panel), upscaled maps (first row of panels), downscaled maps (from the second to the fourth row of panels), and interpolated map (last row of panels) is shown for downscaling/upsampling factors equal to 3, 5, 10, and 30. As the DF increases, some details of the IPWV are lost (compare maps by columns in Fig. 5). Of course, this is more pronounced when the DPFI is used than for the DPMRS case. In addition, it is quite evident that the downscaled maps reveal a variability more pronounced and similar to that of the MERIS map than the

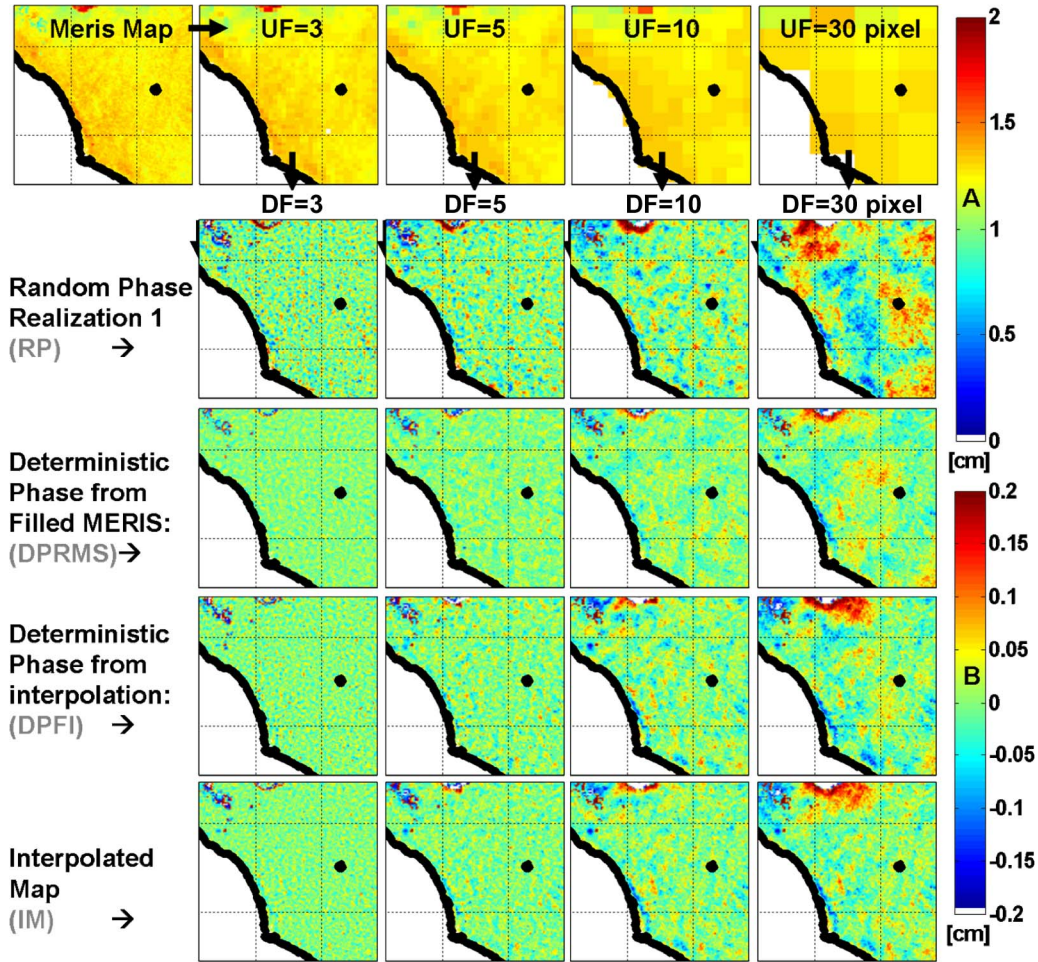


Fig. 5. Qualitative comparison between (upper left) source and downsampled maps for different (DF/UF along different columns) downscaling/upscaling factors and (different rows) downscaling approaches. The term “filled MERIS” in the third row of panels refers to the operation performed on MERIS map to fill the regions where cloud contamination affects the water vapor retrieval. The first row shows the upscaled MERIS reference maps, whereas the other rows show the difference between the downsampled maps (not shown) and the source one shown in the upper left panel. The color bar “A” on the right refers to the maps in the first row; whereas the color bar “B” refers to the rest of the maps.

interpolated ones which, on the contrary, appear to be smoother (i.e., with less information on small-scale variability). This aspect is not surprising since it has been already pointed out in Fig. 4 that the downscaling procedure tends to follow the small-scale variability more accurately than that obtained from the interpolation procedure.

### B. Downscaling of Water Vapor Maps

In this section, a second test on the downscaling procedure is performed. In contrast to what has been shown before, an actual case is considered here. The upscaled field now is given by the MODIS acquisition at a 1-km spatial resolution (instead of the upscaled MERIS as done before). The MODIS acquisition was nearly at the same time as the MERIS one (September 29, 2008, at 09:50 UTC). MERIS remains the reference field. An IPWV data quality check has been performed using the GPS station network available in the target area of Rome at the time of the acquisitions considered in this paper. The quality check has evidenced an appreciable bias of the MODIS observation which has then been removed. On the other hand, rmse accuracy on the order of 0.1 cm, with a bias on the order of 0.01 cm, has

been found for the MERIS observation when compared with GPS [4].

Fig. 6 shows the MERIS (left panel) and MODIS (right panel) acquisitions which appear, on the whole, quite consistent. Thus, the downscaling procedure, in the DPFI configuration, has been run starting from an IPWV field at a 1-km resolution from MODIS to obtain an IPWV field at 250 m (i.e., the same resolution as that from MERIS). Bicubic interpolation has been contextually applied as well. As evident from the lower panels of Fig. 6, the downsampled map (lower left panel), when compared with the MERIS one (upper left corner), characterizes the IPWV variability better than interpolation (lower right panel) which seems not to be able to describe some features of the IPWV field, particularly near the coast.

As emerged in the previous section as well, in this case, the quantitative comparison shown in Table II reveals that error scores (rmse and CC) are slightly better for the interpolation than for power spectral analysis which, on the contrary, favors the downscaling procedure (see the last row of Table II, where the error scores of the difference between PSD from MERIS and both interpolation and downscaling are listed).

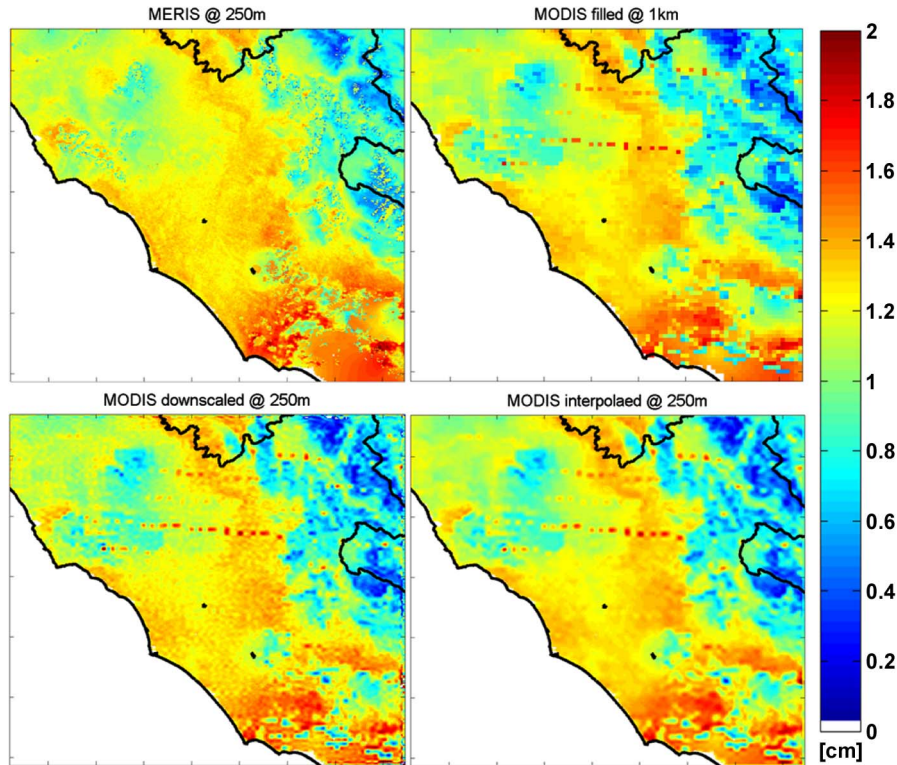


Fig. 6. Upper left: MERIS map at 250 m. Upper right: MODIS at 1 km. Lower left: Downscaled map at 250 m from MODIS at 1 km. Lower right: MODIS at 250 m after applying the cubic interpolation from Matlab. All acquisitions refer to September 29, 2008. White zones in the left corners of each panel correspond to the Tyrrhenian Sea where MERIS and MODIS retrievals are less reliable.

TABLE II  
 ERRORS BETWEEN REFERENCE MERIS IPWV PRODUCTS AT 250 m AND MAPS DERIVED FROM MODIS USING INTERPOLATION AND DOWNSCALING AS WELL AS THE OPTIMAL MODIS PRODUCT AT 1-km RESOLUTION

	Bicubic interpolation (250 m)	Downscaling (250 m)	MODIS (1 km)
RMSE [cm]	0.157	0.165	0.180
CC [cm]	0.830	0.820	0.800
PSD [cm <sup>2</sup> /km]	7.33 10 <sup>5</sup>	5.55 10 <sup>5</sup>	-

To further emphasize the comparison between the down-scaled fields and the target IPWV fields from MERIS, an image texture analysis has been carried out as well.

Texture analysis is based on the calculation of the co-occurrence matrix  $C_{co}$  [21]. In the case of water vapor,  $C_{co}$  represents the distribution of the co-occurring values within the field  $V$ , at a given spatial lag of Cartesian components  $l_x, l_y$ . Formally, the values of the co-occurrence matrix  $C_{co}$  at row  $r$  and column  $c$  of the considered image can be written as follows:

$$C_{co}(r, c) = \sum_{i,j} \begin{cases} 1, & \text{if } V(i, j) = V_r \text{ and } V(i+l_x, j+l_y) = V_c \\ 0, & \text{otherwise} \end{cases} \quad (7)$$

where  $V_r$  and  $V_c$  are generic discrete values of the field  $V(i, j)$ . The square root of the number of elements in  $C_{co}$  defines the number of levels into which the field  $V$  is discretized before computing the co-occurrence matrix  $C_{co}$ . Once  $C_{co}$  is normalized with respect to the total number of co-occurrences, a coprobability matrix  $P_{co}$  is obtained and used to extract some common texture features as

$$C = \sum_{r,c} |r - c|^2 \cdot P_{co}(r, c) \quad (8a)$$

$$E = \sum_{r,c} P_{co}^2(r, c) \quad (8b)$$

$$H = \sum_{r,c} \frac{P_{co}(r, c)}{1 + |r - c|} \quad (8c)$$

where  $C$ ,  $E$ , and  $H$  stand for contrast, energy and homogeneity, respectively, and  $P_{co}(r, c)$  denotes the elements of  $\mathbf{P}$ . When the handled field is constant,  $C = 0$ ,  $E = 1$ , and  $H = 1$ .

Fig. 7 shows the behavior of the texture parameters  $C$ ,  $E$ , and  $H$  as a function of the spatial lag ranging between 0.25 and 5 km, for the detrended reference MERIS map at a 250-m resolution and the downscaled and interpolated MODIS maps at the same resolution. The analysis shown in Fig. 7 demonstrates that all textures extracted from the spectral downscaled output map are closer to those extracted from MERIS than those derived from the interpolated map, particularly at short lag distance.

This result seems to confirm the conclusions drawn before on the basis of the PSD and rmse analysis, which highlighted the tradeoff between the ability of the DPF1 downscaling procedure to reproduce the second-order statistics of the water vapor field quite well at the expense of a slightly worse description of the first-order statistics.

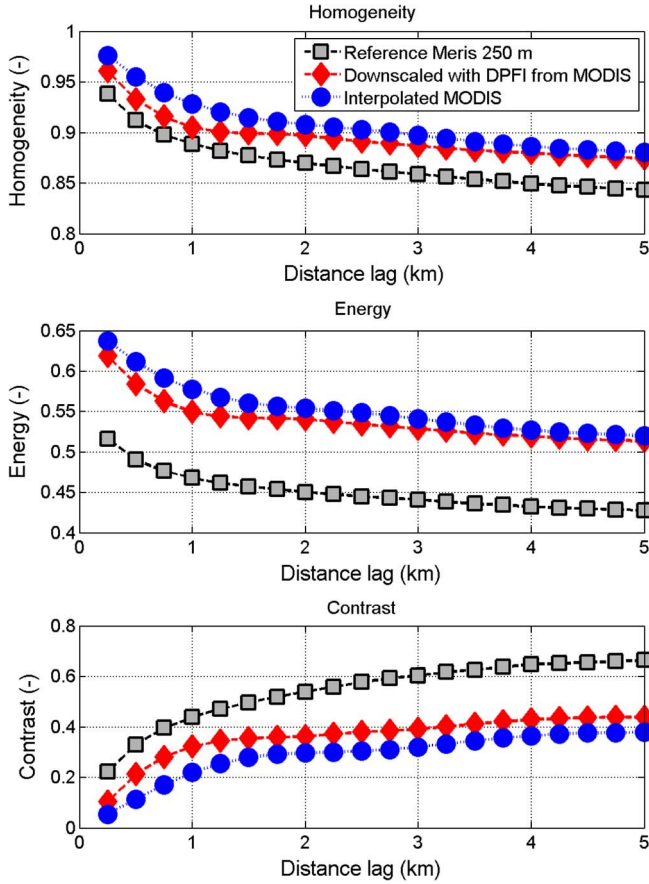


Fig. 7. Texture features, defined in (8), for MERIS at 250-m resolution, MODIS downsampled to 250-m resolution, and MODIS with bicubic interpolation to 250-m resolution. Top panel: Homogeneity  $H$ . Middle panel: Energy  $E$ . Lower panel: Contrast  $C$ .

## V. CONCLUSION

A novel spectral approach to obtain maps of the IPWV field at the desired spatial resolution from IPVW fields at coarser scale (downscaling) has been described. The downscaling algorithm discussed here combines both phase and amplitude information in the Fourier domain, and therefore, it has been labeled as “spectral” downscaling. For this reason, both Fourier phase and amplitude have to be described at unresolved spatial scales. The spectral downscaling proposed here is characterized by the following: 1) the development of a mathematical formulation for modeling the Fourier amplitudes at unresolved scales starting from the variogram characterization of IPVW and leading to a power law small-scale power spectra model and 2) a new way to choose the Fourier phase, based on the interpolation at finer scales (i.e., the DPFI technique).

After applying the downscaling procedure to a coarse resolution map of IPVW, the following results have been emphasized: 1) DPFI downscaling performs much better than the standard RP generation technique; 2) interpolation techniques and spectral DPFI downscaling perform similarly if compared in terms of first-order statistical moment; and 3) spectral downscaling provides better second-order statistics than interpolation does.

On the basis of the aforementioned methodologies and results, it emerges that the spectral downscaling potentially represents a useful tool to reconstruct details that have been lost in

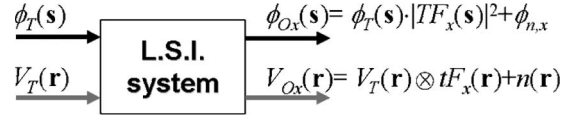


Fig. 8. Model of the observing sensor as an LSI system. Subscripts “ $T$ ” and “ $O$ ” respectively indicate the true and observed quantities from source “ $x$ ,” whereas black and gray arrows respectively indicate space (variable  $\mathbf{r}$ ) and frequency (variable  $\mathbf{s}$ ) descriptions of the same input–output process. The quantity  $n$  is the additive noise.

coarse maps of IPVW. This capability of spectral downscaling is desirable, particularly if it is evaluated in the context of synergy between relatively new sensors, such as SARs, and more conventional instruments, such as MERIS and MODIS, to enhance their observation capability and synergistic use.

## APPENDIX A VARIOGRAM NORMALIZATION

In this appendix, the normalization of the empirical variogram is described. The need for variogram normalization is due to the fact that various sensors, used to observe nearly the same scene, may introduce various errors which, if not removed or at least reduced, may result in misleading conclusions on the observed water vapor field. Namely, if a spatial characterization of water vapor field is needed, the distorting effects introduced by the instrument must be compensated for, or at least mitigated.

This appendix is organized into two sections. The first section deals with the modeling of the noise and spatial filtering introduced by various sensors with respect to the actual water vapor field, whereas the second section is aimed to show how to normalize the variograms for properly comparing observations.

### A. Normalization With Respect to Different Sources of Data

Observations in many cases can be thought of as the result of a linear space-invariant (LSI) process that transforms true “ $T$ ” unknown quantities into observed “ $O$ ” ones (see Fig. 8 for a schematic representation). Assuming the true unknown field as a stationary function of the spatial coordinates, in the spatial frequency domain (variable “ $s$ ”), the observed PSD can be written as follows [22]:

$$\phi_{O,x}(\mathbf{s}) = \phi_T(\mathbf{s}) \cdot |T_{F,x}(\mathbf{s})|^2 + \phi_{n,x}(\mathbf{s}) \quad (\text{A.1})$$

where  $\phi_{O,x}$  and  $\phi_T$  indicate the observed and true power spectral densities of the unknown field observed by sensor  $x$ , respectively, and  $T_{F,x}$  is the system transfer function, whereas  $\phi_{n,x}$  represents an additive noise in the frequency domain, introduced in the observed field by the instrument itself, which can be considered independent on  $\mathbf{s}$  in case of a white noise. As described in Appendix B, from the “true” power spectra density  $\phi_T$ , the “true” variogram  $\gamma_T$  can be easily derived assuming a suitable model, and vice versa. Hereafter, to maintain the treatment simple, the term accounting for the instrumental noise will not be considered.

The characteristics of the LSI system have to be given for each source “ $x$ ” by inferring its transfer function  $T_{F,x}(s)$  in the

frequency domain or its dual impulse response  $t_{F,x}(r)$  in the space domain.

Once  $T_{F,x}(s)$  is defined from linear system theory and if we neglect the noise, the PSD of the true field can be retrieved as

$$\phi_T(\mathbf{s}) = \frac{\phi_{O,x}(\mathbf{s})}{|T_{F,x}(\mathbf{s})|^2}. \quad (\text{A.2})$$

Using the available observations from various sources, it is not feasible to infer the individual quantities  $T_{F,x}(s)$ , but the only strategy may consist in normalizing the various observations in order to make reference to a unique source. In order to do that, we have used as “reference” the IPWV field derived from collocated simulations (in time and space) of the numerical weather forecast mesoscale model (MM5) [23]. Thus, the transfer function  $T'_{F,x}(s)$ , to be used in (A.2), which assumes that the reference MM5 field is the “true,” can be then expressed as

$$|T'_{F,x}(\mathbf{s})| = \left( \frac{\hat{\phi}_{O,x}(\mathbf{s})}{\hat{\phi}_{O,REF}(\mathbf{s})} \right)^{0.5} \quad (\text{A.3})$$

where  $REF = MM5$  and the “upper triangle” above variables indicates estimated quantities. It should be noted that other choices of the reference field are likely practicable, but the lack of instrumental noise in the denominator, which can be ascribed to the MM5 field numerically simulated, is a valuable reason to choose it as reference. Additionally, a numerical model provides regularly spaced values from which a Fourier transform spectral analysis can be done. Conversely, the available observations cannot guarantee the availability of the IPWV at any required position as needed by a Fourier analysis. For this reason, the estimation of the observed and reference power spectral densities  $\phi_{O,x}$  and  $\phi_{O,REF}$  in (A.3) has been accomplished by fitting the semivariograms of the corresponding observations by a power model and using the relationship between the spectral density and the variogram as discussed in Appendix B and described by (3) within the main text.

It is worthwhile to analyze the effect of the sensor on the shape of the variogram of the observed field. Since a sensor can usually be thought of as a system with low-pass characteristics in the spectral domain,  $T_{F,x}$  is expected to decrease as the spatial frequency increases. With reference to the formulation reported in Appendix B, particularly to the relation between variogram  $\gamma$  and covariance functions  $B$  [see (B.1)], it turns out the following equation for the variogram of an observed field when lag distance is greater than zero:

$$\begin{aligned} \gamma_{O,x}(\mathbf{l}) = & \sigma_{n,x}^2 + \int_{-\infty}^{\infty} \int_{-\infty}^{\infty} \phi_T(\boldsymbol{\kappa}) \cdot |T_{F,x}(\boldsymbol{\kappa})|^2 d^2\boldsymbol{\kappa} \\ & - \mathfrak{S}^{-1} \left\{ \phi_T(\boldsymbol{\kappa}) \cdot |T_{F,x}(\boldsymbol{\kappa})|^2 \right\} \quad (\text{A.4}) \end{aligned}$$

where  $\mathbf{k}$  is the spatial wavenumber vector (see Appendix B). The variance of the observed field is the integral of the corresponding spectral density of (A.1) and is formed by the first two terms of the second member of (A.4), with the former representing the variance of the noise  $\sigma_{n,x}^2$ . The third term accounts

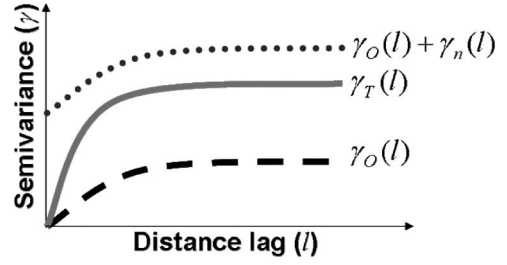


Fig. 9. Theoretical behavior of (gray) true and (black) observed variograms (points) with and (dashed) without instrumental noise.

for the Fourier transform relationship between covariance and spectral density [see (B.3)]. We have neglected the covariance of the noise, which is a Dirac function according to the white noise assumption, and it vanishes at lag distance greater than zero.

From (A.4), it appears that a low-pass  $T_F$  behavior, as expected, reduces the area subtended by the PSD and, thus, the variance of the observed water vapor  $V$ , which corresponds to the plateau value when the semivariogram is represented. This effect is contrasted by the noise, whose variance is added to that of the observation. On the other side, the sharpening of the bandwidth in the frequency domain broadens the covariance function in the lag distance domain. In conclusion, the low-pass behavior results in a reduction of the dynamic of the variogram and a more gently increasing shape, as shown in Fig. 9. The role of instrumental noise is depicted as well by a dotted line representing the sum of a noise-free observed variogram  $\gamma_O$  and the additional constant noise contribution  $\gamma_n = \sigma_n^2$ .

### B. Normalization for Comparing With dInSAR Data

The dInSAR technique provides differential measurements, i.e., differences between observations taken at the same point but at different times.

When dInSAR acquisitions are considered, differences of field values should be introduced in the variogram definition, and (1) becomes

$$\gamma_{\Delta Z}(l) = \frac{1}{2} \cdot \left\langle |\Delta Z(\mathbf{r}+1) - \Delta Z(\mathbf{r})|^2 \right\rangle \quad (\text{A.5})$$

where  $\Delta Z(\mathbf{r}) = Z_1(\mathbf{r}) - Z_2(\mathbf{r})$  and  $Z_1$  and  $Z_2$  are variables sampled at the same position ( $\mathbf{r}$ ) but at different instants and where we have assumed to deal with isotropic fields. Explicating the difference in (A.5) and rearranging, we have the following terms:

$$\begin{aligned} \gamma_{\Delta Z}(l) = & \frac{1}{2} \left\langle |Z_1(\mathbf{r}+1) - Z_1(\mathbf{r})|^2 \right\rangle + \frac{1}{2} \left\langle |Z_2(\mathbf{r}+1) - Z_2(\mathbf{r})|^2 \right\rangle + \\ & - \langle [Z_1(\mathbf{r}+1) - Z_1(\mathbf{r})][Z_2(\mathbf{r}+1) - Z_2(\mathbf{r})] \rangle. \quad (\text{A.6}) \end{aligned}$$

If the field is stationary in time, the variogram functions of  $Z_1$  and  $Z_2$  are identical and equal to  $\gamma_Z(l)$ . Assuming that samples taken at different instants are not correlated with each other, the third term in the second member contains terms of type  $\langle Z_1 \cdot Z_2 \rangle$  and thus vanishes so that (A.6) is formally identical to (1) except for a factor 2

$$\gamma_{\Delta Z}(l) = 2\gamma_Z(l). \quad (\text{A.7})$$

The factor 2 is needed when  $\gamma_{\Delta Z}$  has to be compared with  $\gamma_Z$ .

## APPENDIX B POWER SPECTRA FROM SEMIVARIOGRAM

This appendix gives the mathematical formulation to derive the PSD from the variogram description of the handled field, as indicated in (3) within the main text.

Usually semivariograms, defined as in (1), provide a 1-D information of the correlation structure of data. Roughly speaking, this means that variograms and correlations describe the same property differently. Assuming a second-order stationarity (i.e., the mean does not depend on the position and the covariance depends on the distance between two positions, which also implies that the variance does not depend on position), it can be easily demonstrated that, for a generic geophysical field  $Z$  assumed as a random function, the following relation between covariance function ( $B$ ) and variogram ( $\gamma$ ) holds:

$$B_Z(\mathbf{l}) = \sigma_Z^2 - \gamma_Z(\mathbf{l}) \quad (\text{B.1})$$

where  $\mathbf{l}$  is the lag distance vector of component  $l_x, l_y$  and  $\sigma^2$  indicates the variance. The PSD, as well known, represents another way to study the spatial correlation of data, and it is calculated by taking the Fourier transform (operator  $\mathfrak{F}$ ) of the covariance function  $B$  as follows:

$$\phi_Z(\mathbf{s}) = \mathfrak{F}\{B_Z(\mathbf{l})\} \quad (\text{B.2})$$

where  $\mathbf{s}$  is the spatial frequency vector of components  $s_x$  and  $s_y$ . Expressing (B.2) in the Cartesian domain, it gives

$$\phi_Z(\mathbf{s}) = \int_{-\infty}^{\infty} \int_{-\infty}^{\infty} B_Z(l_x, l_y) \cdot e^{-j\kappa_x l_x} \cdot e^{-j\kappa_y l_y} dl_x dl_y \quad (\text{B.3})$$

where the spatial wavenumbers  $\kappa_x$  and  $\kappa_y$  are defined as  $2\pi s_x$  and  $2\pi s_y$ , respectively, and  $s_x$  and  $s_y$  are the spatial frequencies. Assuming from now on that the field is azimuthally isotropic, (B.3) can be conveniently expressed in polar coordinates ( $l, \varphi$  for the lag distance and  $\kappa, \theta$  for the wavenumbers), considering the Jacobian of the transformation and expressing both  $l_x, l_y$  and  $\kappa_x, \kappa_y$ , respectively, as  $l_x = l \cdot \cos \varphi$ ,  $l_y = l \cdot \sin \varphi$ ,  $\kappa_x = \kappa \cdot \cos \theta$ ,  $\kappa_y = \kappa \cdot \sin \theta$

$$\phi_Z(\mathbf{s}) = \int_0^{\infty} \int_0^{2\pi} B_Z(l, \varphi) \cdot l \cdot e^{-j\kappa l (\cos \theta \cos \varphi + \sin \theta \sin \varphi)} dl \cdot d\varphi. \quad (\text{B.4})$$

Making the assumption of spatial isotropy, the dependence of the covariance function on angle  $\varphi$  vanishes. Remembering the addition and subtraction trigonometric formulas (i.e.,  $\cos(\theta - \varphi) = \cos \theta \cdot \cos \varphi + \sin \theta \cdot \sin \varphi$ ), (B.4) becomes

$$\phi_Z(\mathbf{s}) = \int_0^{\infty} \int_0^{2\pi} B_Z(l) \cdot l \cdot e^{-j\kappa l \cos(\theta - \varphi)} dl \cdot d\varphi. \quad (\text{B.5})$$

From (B.5), the integral with respect to the angle  $\varphi$  of the exponential is recognized to be equal to  $2\pi$  times the Bessel

function of the first kind of order zero  $J_0(k \cdot l)$ . Note that  $J_0(k \cdot l) = J_0(-k \cdot l)$  since  $J_0$  is an even function about zero. According to these considerations, (B.5) can be written as

$$\phi_Z(\mathbf{s}) = 2\pi \cdot \int_0^{\infty} B_Z(l) \cdot l \cdot J_0(k \cdot l) \cdot dl = 2\pi \cdot H_0\{B_Z(l)\} \quad (\text{B.6})$$

where the integral in (B.6) is the definition of the Hankel transform of order zero ( $H_0$ ) of the spatially isotropic covariance function  $B_Z(l)$ .

Considering (B.1), the covariance can be expressed as a function of variograms, so that the PSD results in the sum of two Hankel transform terms as specified in the following:

$$\phi_Z(\mathbf{s}) = 2\pi \cdot (H_0\{\sigma_Z^2\} - H_0\{\gamma_Z(l)\}) \quad (\text{B.7})$$

where the term  $H_0(\sigma_Z^2)$  can be approximated as

$$H_0\left\{\sigma_Z^2 \cdot \text{rect}\left(\frac{l}{p}\right)\right\} = \sigma_Z^2 \cdot p^2 \cdot \frac{J_1(2\pi s \cdot p)}{2\pi s \cdot p}. \quad (\text{B.8})$$

In (B.8), we assumed that the upper limit of the integral in (B.6) is limited to  $p$ , i.e., through the introduction of the “*rect*” operator, that the term  $\sigma_Z^2$  is constant within the spatial interval  $[0, p]$  and 0 elsewhere with the parameter  $p$  as large as possible. From Bessel function-related formulations [30], we recognize the term of the type  $J_1(u)/u$  (with  $u = p \cdot s$  and  $J_1$  being the Bessel function of the first kind and order 1) to be the “*jinc*” function that is a decreasing oscillating function with a maximum equal to 0.5 in  $u = 0$  and the first secondary maximum at  $u = \pm 3.83$ . As the parameter  $p$  increases,  $J_1(u)/u$  tends to give a contribution only in the origin of the reference system, i.e.,  $s = 0$ . For this reason, it is neglected at the smaller spatial scales that we want to model (i.e., for larger values of spatial frequency  $s$ ).

The second term in (B.7), in the case of water vapor field, can be replaced by the power law model  $\gamma_{PL}$  formalized in (2) within the main text. However, the power law function does not admit the Hankel transform since it is not summable. To overcome this problem, we modified  $\gamma_{PL}$  in (2) as follows:

$$\gamma_{PL}(l) \cong J_0(a \cdot l) \cdot l^b = \gamma_{BL}(l) \quad (\text{B.9})$$

where  $a$  and  $b$  are coefficients which can be chosen so that  $\gamma_{PL}$  approximates  $\gamma_{BL}$ . For instances considering the power law fit, the empirical semivariograms  $\gamma_{PL}$  having  $a = 0.19 \cdot 10^{-7}$  and  $b = 0.37$  are very close to  $\gamma_{BL}$ , where the maximum difference is equal to 1% for distance lags less than 50 km.

Thus, the third term of (B.7), considering  $\gamma_{BL}$  instead of  $\gamma_{PL}$ , can be expressed as shown in the following [31]:

$$H_0\{\gamma_{BL}(l)\} = \begin{cases} C_1(a, b) \cdot (s^2 - a^2)^{-b-1} & \text{for } s > a \\ 0 & \text{for } 0 < s \leq a \end{cases} \quad (\text{B.10})$$

where  $C_1$  is a constant value given by

$$C_1(a, b) = \frac{2^{b+1} \cdot a^b}{\Gamma(-b)}. \quad (\text{B.11})$$

In (B.11),  $\Gamma$  is the gamma function. Substituting (B.8), (B.10), and (B.11) into (B.7), (3) within the main text is

obtained when  $Z = V$ . Note that, at higher spatial frequencies (so that  $s \gg a$  and  $p \gg 3.83/a$ ), the contribution in (B8) vanishes and the spectral density becomes proportional to  $s^{-\nu}$ , with  $\nu = 2b + 2$

$$\phi_Z(s) \approx -\frac{C_1(a, b)}{s^{2b+2}} \quad s \gg a. \quad (\text{B.12})$$

ACKNOWLEDGMENT

The authors would like to thank the Mitigation of Electromagnetic Transmission errors induced by Atmospheric Water Vapor Effects project teams for the useful cooperation and data preprocessing. In particular, the authors would like to thank Dr. S. Bonafoni for collecting the Medium Resolution Imaging Spectrometer and Moderate Resolution Imaging Spectroradiometer observations, Dr. D. Cimini for producing the integrated water vapor from these acquisitions, Dr. A. Mazzoni for collecting the Global Positioning System data and producing the *zenith total delay* values, Prof. P. Ciotti for retrieving the *zenith wet delay* values, Prof. R. Ferretti and her staff for running the Mesoscale Model 5 model, and the staff of the Polytechnic University of Milan, particularly Prof. F. Rocca for his useful suggestions and Dr. D. Perissin for the atmospheric phase screen maps. The authors would also like to thank the European Space Agency (ESA) staff and the study manager Dr. B. Rommen. The work has been carried out under the ESA/European Space research and TEchnology Centre contract N, 21207/07/NL/HE.

REFERENCES

[1] J. C. Alishouse, S. A. Snyder, J. Vongsathorn, and R. R. Ferraro, "Determination of oceanic total precipitable water from the SSM/I," *IEEE Trans. Geosci. Remote Sens.*, vol. 28, no. 5, pp. 811–816, Sep. 1990.

[2] C. B. Blankenship, A. Al-Khalaf, and T. T. Wilheit, "Retrieval of water vapor profiles using SSM/T-2 and SSM/I data," *J. Atmos. Sci.*, vol. 57, no. 7, pp. 939–955, Apr. 2000.

[3] M. N. Deeter and K. F. Evans, "Mesoscale variations of water vapour inferred from millimeter-wave imaging radiometer during TOGA COARE," *J. Appl. Meteorol., Notes Corresp.*, vol. 36, no. 2, pp. 183–188, Feb. 1997.

[4] Z. Li, J. P. Muller, P. Cross, P. Albert, J. Fischer, and R. Bennartz, "Assessment of the potential of MERIS near-infrared water vapour products to correct ASAR interferometric measurements," *Int. J. Remote Sens.*, vol. 27, no. 2, pp. 349–365, Jan. 2006.

[5] Y. J. Kaufman and B.-C. Gao, "Remote sensing of water vapor in the near IR from EOS/MODIS," *IEEE Trans. Geosci. Remote Sens.*, vol. 30, no. 5, pp. 871–884, Sep. 1992.

[6] N. Rebora, L. Ferraris, J. von Hardenberg, and A. Provenzale, "The RainFARM: Rainfall downscaling by a filtered autoregressive model," *J. Hydrometeorology*, vol. 7, no. 4, pp. 724–738, 2006.

[7] R. Huth, "Downscaling of humidity variables: A search for suitable predictors and predictands," *Int. J. Climatol.*, vol. 25, no. 2, pp. 243–250, 2005.

[8] J. P. Kahane, "Sur le modele de turbulence de Benoit Mandebrot," *Comptes Rendus*, vol. 278A, pp. 621–623, 1974.

[9] L. Ferraris, S. Gabellani, N. Rebora, and A. Provenzale, "A comparison of stochastic models for spatial rainfall downscaling," *Water Resour. Res.*, vol. 39, no. 12, pp. 1368–1384, 2003.

[10] J. Mejia and I. Rodriguez-Iturbe, "On the synthesis of random fields sampling from the spectrum: An application to the generation of hydrologic spatial processes," *Water Resour. Res.*, vol. 10, no. 4, pp. 705–711, 1974.

[11] T. L. Bell, "A space-time stochastic model of rainfall for satellite remote sensing studies," *J. Geophys. Res.*, vol. 92, no. D8, pp. 9631–9643, 1987.

[12] G. Guillot and T. Lebel, "Disaggregation of Sahelian mesoscale convective system rain fields: Further developments and validation," *J. Geophys. Res.*, vol. 104, no. D24, pp. 31 533–31 551, 1999.

[13] N. Pierdicca, F. S. Marzano, F. Rocca, D. Perissin, P. Basili, S. Bonafoni, V. Mattioli, D. Cimini, P. Ciotti, R. Ferretti, M. Montopoli, W. Foster, R. Notarpietro, S. Padmanabhan, E. Pichelli, S. Reising, S. Sahoo, and G. Venuti, "Atmospheric water-vapour effects on spaceborne Interferometric SAR imaging: Data synergy and comparison with ground-based measurements and meteorological model simulations at urban scale," in *Proc. 3rd Eur. Conf. Antennas Propag.*, Berlin, Germany, Mar. 2009, pp. 3443–3447.

[14] H. Wackernagel, *Multivariate Geostatistics*, 2nd ed. Berlin, Germany: Springer-Verlag, 1998.

[15] P. Basili, S. Bonafoni, V. Mattioli, P. Ciotti, and N. Pierdicca, "Mapping the atmospheric water vapor by integrating microwave radiometer and GPS measurements," *IEEE Trans. Geosci. Remote Sens.*, vol. 42, no. 8, pp. 1657–1665, Aug. 2004.

[16] J. Morland and C. Mätzler, "Spatial interpolation of GPS integrated water vapour measurements made in the Swiss Alps," *Meteorol. Appl.*, vol. 14, no. 1, pp. 15–26, Mar. 2007.

[17] S. Williams, Y. Bock, and P. Fang, "Integrated satellite interferometry: Troposphere noise, GPS estimates, and implications for synthetic aperture radar products," *J. Geophys. Res.*, vol. 103, no. B11, pp. 27 051–27 067, 1998.

[18] V. I. Tatarskii, *The Effects of the Turbulent Atmosphere on Wave Propagation*. Jerusalem, Israel: Israel Program Sci. Transl., 1971, 472 pp.

[19] O. P. Lay, "The temporal power spectrum of atmospheric fluctuations due to water vapor," *Astron. Astrophys. Suppl. Ser.*, vol. 122, pp. 535–545, May 1997.

[20] M. Montopoli and F. S. Marzano, "Spatial characterization and downscaling of rain attenuation fields from numerical weather prediction models," in *Proc. 3rd Eur. Conf. Antennas Propag.*, Berlin, Germany, Mar. 2009, pp. 318–322.

[21] R. M. Haralick and K. Shanmugam, "Textural features for image classification," *IEEE Trans. Syst., Man, Cybern.*, vol. SMC-3, no. 6, pp. 610–621, Nov. 1973.

[22] S. Haykin, *Adaptive Filter Theory*, 3rd ed. Englewood Cliffs, NJ: Prentice-Hall, 1996, ser. Prentice Hall Information and System Sciences Series, p. 136.

[23] E. Pichelli, R. Ferretti, D. Cimini, D. Perissin, M. Montopoli, F. S. Marzano, and N. Pierdicca, "Water vapour distribution at urban scale using high-resolution numerical weather model and spaceborne SAR interferometric data," *Nat. Hazards Earth Syst. Sci.*, vol. 10, no. 1, pp. 121–132, 2009.

[24] V. Venema, S. G. Garcia, and C. Simmer, "A new algorithm for the downscaling of cloud fields," *Q. J. R. Meteorol. Soc.*, vol. 136, no. 646, pt. A, pp. 91–106, Jan. 2010.

[25] V. Venema, S. Meyer, S. Gimeno Garcia, A. Kniffka, C. Simmer, S. Crewell, U. Löhnert, T. Trautmann, and A. Macke, "Surrogate cloud fields generated with the iterative amplitude adapted Fourier transform algorithm," *Tellus A*, vol. 58, no. 1, pp. 104–120, Jan. 2006.

[26] A. Ferretti, C. Prati, and F. Rocca, "Permanent scatterers in SAR interferometry," *IEEE Trans. Geosci. Remote Sens.*, vol. 39, no. 1, pp. 8–20, Jan. 2001.

[27] R. Dach, P. Steigenberger, S. Schaer, and M. Fritsche, "The Bernese Software in the reprocessing environment," in *Proc. IGS Workshop*, Newcastle upon Tyne, U.K., Jun. 28–Jul. 2, 2010.

[28] J. Saastamoinen, "Atmospheric correction for the troposphere and stratosphere in radio ranging of satellites," in *Use of Artificial Satellites for Geodesy*, vol. 15, S. W. Henriksen, A. Mancini, and B. H. Chovitz, Eds. Washington, DC: AGU, 1972, ser. Geophys. Monogr. Ser., pp. 247–251.

[29] R. Bennartz and J. Fischer, "Retrieval of columnar water vapour over land from back-scattered solar radiation using the Medium Resolution Imaging Spectrometer (MERIS)," *Remote Sens. Environ.*, vol. 78, no. 3, pp. 274–283, Dec. 2001.

[30] R. N. Bracewell, *Fourier Analysis and Imaging*. New York: Springer-Verlag, 2003, pp. 352–363.

[31] A. D. Poularikas, Ed., *The Transforms and Applications Handbook*, 2nd ed. Boca Raton, FL: CRC Press, 2000, ch. 9, table 9.2.

[32] F. Onn and H. A. Zebker, "Correction for interferometric synthetic aperture radar atmospheric phase artifacts using time series of zenith wet delay observations from a GPS network," *J. Geophys. Res.*, vol. 111, p. B09102, 2006. doi:10.1029/2005JB004012.

[33] Z. Li, J. P. Muller, and P. Cross, "Tropospheric correction techniques in repeat-pass SAR interferometry," in *Proc. FRINGE Workshop (ESA SP-550)*, H. Lacoste, Ed., Dec. 1–5, 2003, p. 51.1, [CD-ROM].

[34] Y. H. Kaheil and I. F. Creed, "Detecting and downscaling wet areas on boreal landscapes," *IEEE Geosci. Remote Sens. Lett.*, vol. 6, no. 2, pp. 179–183, Apr. 2009.



**Mario Montopoli** received the Laurea degree in electronic engineering from the University of L'Aquila, L'Aquila, Italy, in 2004, and the Ph.D. degree in radar meteorology in a joint program between the University of Basilicata, Potenza, Italy, and the Sapienza University of Rome, Rome, Italy, in 2008.

In 2005, he joined the Centro di Eccellenza per l'integrazione di Tecniche di Telerilevamento e Modellistica Numerica per la Previsione di Eventi Meteorologici Severi as a Research Scientist on ground-based radar meteorology with a special focus

on C-band applications and processing techniques. Since 2006, he has been with the Department of Electrical and Information Engineering, University of L'Aquila, as a Research Assistant.

Dr. Montopoli was the recipient of the best paper award in the European Radar Conference held in Sibiu (Romania) in 2010.



**Nazzareno Pierdicca** received the Laurea (Doctor's) degree in electronic engineering (*cum laude*) from the University "La Sapienza" of Rome, Rome, Italy, in 1981.

In 1978–1982, he worked for the Italian Agency for Alternative Energy (ENEA). From 1982 to 1990, he has been working with Telespazio, Rome, in the Remote Sensing Division. In November 1990, he joined the Department of Information, Electronic and Telecommunication Engineering, Sapienza University of Rome. He is currently an Associate Professor

and teaches remote sensing and electromagnetic fields at the Faculty of Engineering, Sapienza University of Rome. His research activity mainly concerns electromagnetic scattering and emission models for sea and bare soil surfaces and their inversion, microwave radiometry of the atmosphere, and radar land applications.

Dr. Pierdicca is a member of the IEEE Geoscience and Remote Sensing Society (GRSS) and a past Chairman of the GRSS Central Italy Chapter.



**Frank Silvio Marzano** (S'89–M'99–SM'03) received the Laurea degree (*cum laude*) in electrical engineering and the Ph.D. degree in applied electromagnetics from the Sapienza University of Rome, Rome, Italy, in 1988 and 1993, respectively.

In 1993, he was with the Institute of Atmospheric Physics, National Research Council, Rome. From 1994 to 1996, he was with the Italian Space Agency, Rome, as a Postdoctorate Researcher. In 1997, after being a Lecturer with the University of Perugia, Perugia, Italy, he joined the Department of Electrical

Engineering and cofounded the Centro di Eccellenza per l'integrazione di Tecniche di Telerilevamento e Modellistica Numerica per la Previsione di Eventi Meteorologici Severi, University of L'Aquila, L'Aquila, Italy, coordinating the Satellite and Radar Remote Sensing Laboratory. Since 2005, he has been with the Department of Information, Electronic and Telecommunication Engineering, Sapienza University of Rome, where he currently teaches courses on antennas, propagation, and remote sensing. His current research concerns passive and active remote sensing of the atmosphere from ground-based, airborne, and spaceborne platforms, with a particular focus on precipitation using microwave and infrared data, development of inversion methods, radiative transfer modeling of scattering media, and radar meteorology issues. He is also involved in radiopropagation topics in relation to incoherent wave modeling, scintillation prediction, and rain fading analysis along satellite microwave links.

Dr. Marzano was the recipient of the Young Scientist Award of the XXIV Union Radio Scientifique Internationale General Assembly in 1993 and the Alan Berman Research Publications Award from the Naval Research Laboratory, Washington, DC, in 1998. Since 2001, he has been the Italian national delegate for the European Cooperation in the Field of Scientific and Technical Research Actions 720 and 280. Since January 2004, he has been acting as an Associate Editor of the IEEE GEOSCIENCE AND REMOTE SENSING LETTERS.